

Recent Results from the RICE Experiment at the South Pole

I. Kravchenko,¹ D. Seckel,² J. Adams,³ A. Baird,³ S. Churchwell,³ P. Harris,³ S. Seunarine,³ A. Bean,⁴ D. Besson,⁴ K. Byleen-Higley,⁴ S. Chambers,⁴ J. Drees,⁴ S. Graham,⁴ D. McKay,⁴ J. Meyers,⁴ L. Perry,⁴ J. Ralston,⁴ J. Snow,⁴ S. Razzaque⁵

(1) *M.I.T. Lab. for Nuclear Science, Cambridge, MA 02139*

(2) *Bartol Research Institute, U. of Delaware, Newark DE 19716*

(3) *Department of Physics and Astronomy, Private Bag 4800, U. of Canterbury, Christchurch, New Zealand*

(4) *KU Dept. of Physics and Astronomy, Lawrence KS 66045*

(5) *Pennsylvania State University, University Park, PA 16802*

We present a compilation of recent results, submitted to the 2003 International Cosmic Ray Conference (Tsukuba, Japan). These include: a) Revised Monte Carlo estimates of the radiofrequency signals produced by electromagnetic showers in ice, b) an updated search for ultra-high energy (UHE) neutrinos based on detection of radio-wavelength Cherenkov radiation; such radiation results from neutrino-induced electromagnetic showers in cold Polar ice, and c) An *in situ* measurement of the index of refraction through the South Polar firn.

I. INTRODUCTION AND METHODS

The Antarctic icecap has provided an extraordinary laboratory for a variety of scientific purposes. The AMANDA, IceCube [1], ANITA [2], and RICE collaborations seek to use the dense, solid, large-volume, and extraordinarily transparent [3] (for $\lambda > 100$ nm) icecap as a neutrino target; the pioneering AMANDA experiment has successfully demonstrated the viability of in-ice optical detection of atmospheric neutrinos, through the reconstruction of hundreds of muon neutrinos. All these experiments seek to measure UHE neutrinos by detection of Cherenkov radiation produced by $\nu_l + N \rightarrow l + N'$. Whereas AMANDA/IceCube is optimized for detection of penetrating muons resulting from $\nu_\mu + N \rightarrow \mu + N'$, RICE/ANITA are designed to detect compact electromagnetic cascades initiated by $e^+(/e^-)$: $\nu_e(/ \bar{\nu}_e) + N \rightarrow e^\pm + N'$. As the cascade develops, atomic electrons in the target medium are swept into the forward-moving shower, resulting in a net charge on the shower front of $Q_{tot} \sim E_s e/4$; E_s is the shower energy in GeV. Such cascades produce broadband Cherenkov radiation – for $\lambda_{E-field}^{Cherenkov} > r_{Moliere}$, the emitting region approximates a point charge of magnitude Q_{tot} and therefore emits fully coherently; fortuitously, the field attenuation length at such wavelengths ≥ 1 km. One calculation finds that, for $1 \text{ PeV} < E_{\nu_e}$, radio detection of cascades becomes more cost-effective than PMT-based techniques [4].

The RICE experiment consists of an array of 20 in-ice dipole receivers, deployed at depths of 100 – 400 m, and read out into digital oscilloscopes. Calibration techniques and event reconstruction, as well as results on the neutrino flux at earth, are presented elsewhere [6]. An initial ν_e -only analysis based on data taken in August, 2000 has been presented elsewhere [5]. Using calculations presented herein of the expected radio-frequency signal strength due to an electromagnetic shower, the measured RICE hardware performance, reconstruction software and simulation [6], we now report on an expanded neutrino search based on all data taken in 1999, 2000, and 2001. We additionally use the excellent timing characteristics of the RICE receiver array to measure the electromagnetic wave speed through the firn.

II. EXPERIMENTAL DESCRIPTION

The RICE experiment presently consists of a 20-channel array of dipole radio receivers (“Rx”), scattered within a 200 m×200 m×200 m cube, at 100-300 m depths. The signal from each antenna is boosted by a 36-dB in-ice amplifier, then carried by coaxial cable to the surface observatory, where the signal is filtered (suppressing noise below 200 MHz), re-amplified (either 52- or 60-dB gain), and split - one copy is fed into a CAMAC crate to form the event trigger; the other signal copy is routed into one channel of an HP54542 digital oscilloscope. Short-duration pulses broadcast from under-ice transmitters provide the primary calibration signals, and are used to verify vertex reconstruction techniques. Figure 1a) illustrates the vertex reconstruction performance for our calibration transmitter data (transmitters are typically 100-200 m from receivers) using two vertex-reconstruction algorithms. One algorithm searches a cubic km. grid around the array for the source point most consistent with the observed hit times; the second technique

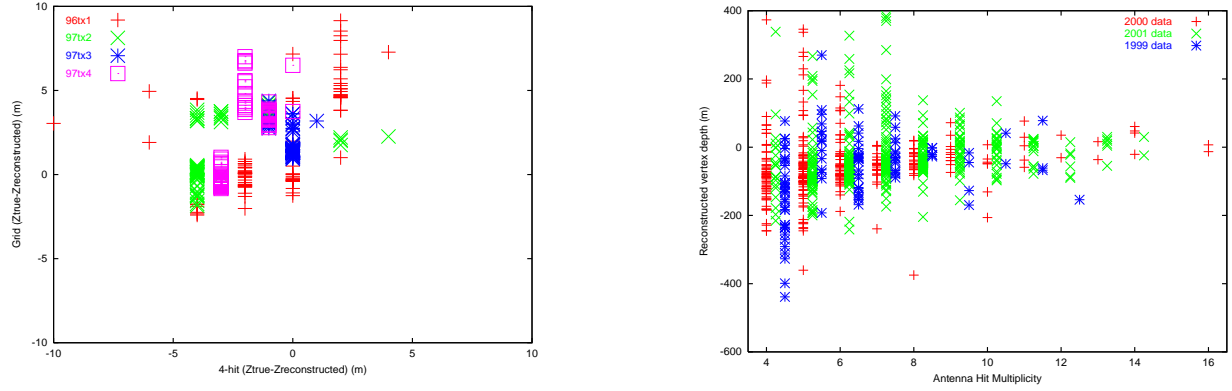


FIG. 1. Left (a): Deviation between true depth and reconstructed depth for four separate transmitters, for the two source reconstruction codes; Right (b): Raw distribution of reconstructed z-vertex vs. hit multiplicity for 1999, 2000, 2001 data, using analytic vertex reconstruction algorithm. No ray-tracing corrections for transmission through the firm have been made, which accounts for much of the scatter in the data, nor have quality-of-fit cuts been applied. Each point represents ~ 50 events.

analytically solves for the vertex using four-hit subcombinations of all the available hits. Typical differences between reconstructed and known depths are of the order a few meters. For non-calibration events, we expect reconstructed source vertices to cluster around the surface; smearing effects due to ray tracing through the firm may be considerable. Figure 1b) displays the reconstructed source depth for our “general” triggers for various hit multiplicities; source depths are observed to peak towards $z=0$ (consistent with surface anthropogenic activity).

With newer data, and after applying variable index-of-refraction corrections, the reconstructed source depth distribution typically sharpens, as shown in Figure 2.

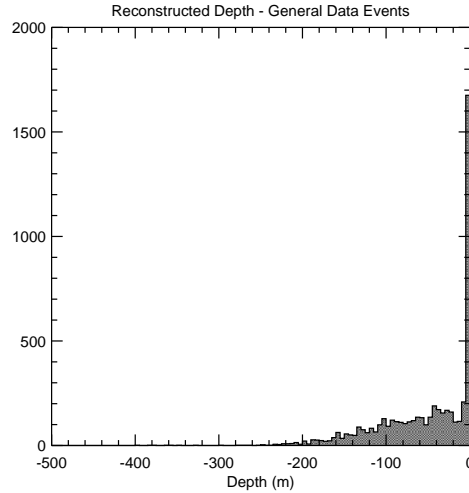


FIG. 2. Reconstructed vertex depths for 5/1/03→5/10/03 RICE data; the majority of events are consistent with a surface origin.

TABLE I. Track length and particle yield results from an averaged 100 GeV electron-induced shower using different Monte Carlo shower codes. The error bars correspond to error in the mean, s/\sqrt{N} , where s is the standard deviation and N is the number of showers (100 for GEANT 4 and 20 in all other cases).

Shower code	Total track lengths			Particle yield at shower max	
	Absolute ($e + p$) [m]	Projected ($e + p$) [m]	Projected ($e - p$) [m]	($e + p$)	($e - p$)
G3 (preferred)	542.74 ± 0.08	455.3 ± 0.2	125.0 ± 2.0	148 ± 5	42 ± 3
G3 (default)	389.51 ± 0.48	365.7 ± 0.5	76.3 ± 1.5	111 ± 7	20 ± 2
G4	572.58 ± 0.04	466.3 ± 0.2	135.0 ± 0.8	153 ± 3	45 ± 1
ZHS	642.17 ± 0.06	516.6 ± 0.2	135.2 ± 1.5	164 ± 6	44 ± 2

III. GEANT-BASED CALCULATIONS OF RF CHERENKOV SIGNAL STRENGTHS

A. Background

Ultrahigh energy electron neutrinos from cosmological sources can be detected from the shower created in dense media (ice e.g.) by the secondaries in a charged current interaction ($N\nu_e \rightarrow eX$). Shower particles travelling faster than light in the medium emit coherent Cherenkov signals at radio frequencies, which are detected by radio antennas buried in the medium.

We have modeled the signal contribution from the dominant ($\sim 80\%$) electromagnetic shower component using GEANT detector simulation tools. Shower simulation and electromagnetic pulse generation from shower particles are essentially two separate procedures in our study. The details of our previous studies can be found elsewhere [7]. We report here highlights of our recent efforts.

B. Shower Simulations

We have defined a cube of ice of km scale as the target medium in our GEANT simulations. Given an effective atomic number $Z = 7.2$, an effective mass $A = 14.3$ and a density 0.92 g/cm^3 of the medium, GEANT calculates all necessary parameters (radiation length, absorption length and cross-sections, e.g.) internally.

The electromagnetic showers, in our analysis, are initiated by an e^- or γ with pre-specified momenta and position. GEANT gives detailed particle tracking information such as interaction points, total energy, energy lost in interaction and interaction time in output data files. These data files are used later to calculate electromagnetic pulses and to diagnose shower properties.

We used GEANT 3.21 and, more recently, GEANT 4 to simulate electromagnetic showers in ice. In our original work [7], we used GEANT 3.21 with default settings to generate showers, which yields significantly less track length compared to GEANT 4 and to GEANT 3.21 with “preferred” settings. The reason is that, with the default setting, electrons are stopped prematurely before reaching the low kinetic energy threshold needed for accurate Cherenkov radio signal emission calculations. Our updated results from GEANT 3.21 with preferred settings and GEANT 4 are in reasonable agreement with each other and with other results [8–11]. In the lower frequency range, the signal is significantly increased compared to the signal reported earlier. Total track lengths and particle yields at the shower maximum are reported in Table I for an average 100 GeV e^- shower generated by GEANT 3.21 with the preferred and default settings and GEANT 4. Also shown are results from our copy of the Zas, Halzen and Stanev [8] code for comparison.

C. Calculation of Radio Signal

We have calculated the net electric field, in the Fraunhofer limit, by vector superposing contributions from Monte Carlo track segments of all the charged particle using the formula:

$$R\vec{E}_\omega(\vec{x}) = \frac{1}{\sqrt{2\pi}} \left(\frac{\mu_r q}{c^2} \right) e^{ikR} e^{i\omega[t_1 - (n/c)\hat{n} \cdot \vec{r}_1]} \vec{v}_\perp \frac{e^{i\omega\delta t(1 - \hat{n} \cdot \vec{\beta}n)} - 1}{1 - \hat{n} \cdot \vec{\beta}n} \quad (1)$$

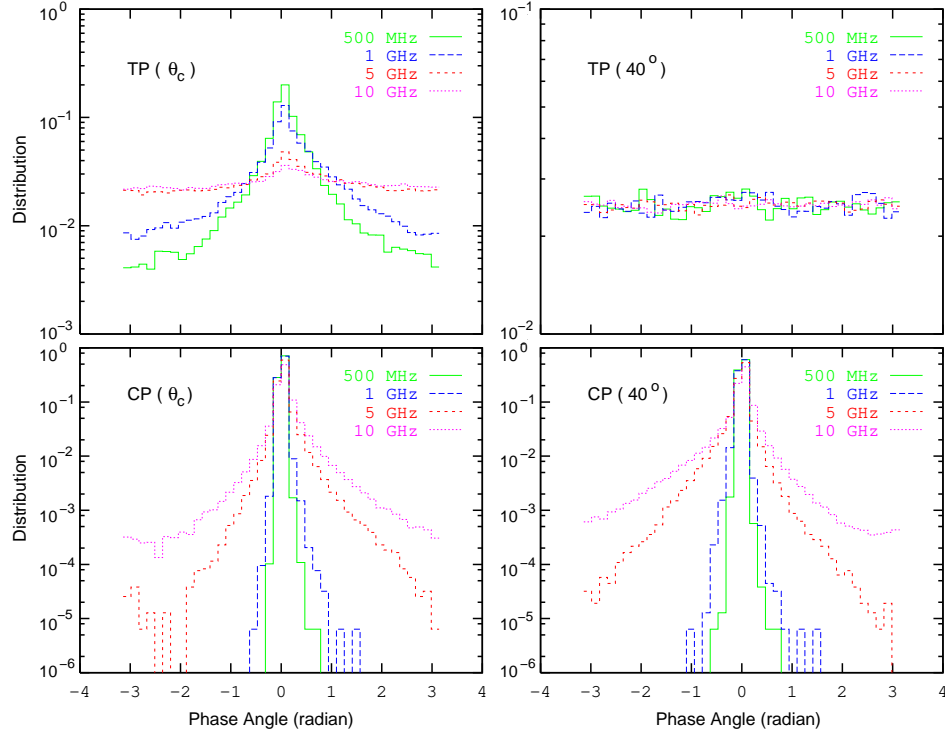


FIG. 3. Translational phase (TP) [top panels] and the Cherenkov phase (CP) [bottom panels] distributions at the Cherenkov [left panels] and 40° angle [right panels] for a 100 GeV shower. The TP is the determining factor in coherent signal emissions.

where (t_1, \vec{r}_1) is the initial position of a track segment and δt is the time elapsed. The refractive index of the medium is denoted by n and $\vec{v}_\perp = -\hat{n} \times (\hat{n} \times \vec{v})$, \vec{v} being the particle velocity and \hat{n} the observer's direction. The condition $1 - \hat{n} \cdot \vec{\beta}n = 0$ defines signal emission at the Cherenkov angle $\theta_c = \cos^{-1}(1/n\beta)$. At or close to this angle Eq. (1) reduces to

$$R\vec{E}_\omega(\vec{x}) = \frac{i\omega}{\sqrt{2\pi}} \left(\frac{\mu_r q}{c^2} \right) e^{ikR} e^{i\omega[t_1 - (n/c)\hat{n} \cdot \vec{r}_1]} \vec{v}_\perp \delta t. \quad (2)$$

A study of the phase angles: $\omega[t_1 - (n/c)\hat{n} \cdot \vec{r}_1]$ and $\omega\delta t(1 - \hat{n} \cdot \vec{\beta}n)$ (the translational phase (TP) and the Cherenkov phase (CP) respectively) shows that coherent signal emission is dominated by TP (see Fig. 3). These uncorrelated phases allow one to factorize the field equations and calculate the electric field semi-analytically by parametrizing the shower with a form-factor. This serves as a check of our understanding of the frequency spectrum of the electric field at the Cherenkov angle calculated by the direct Monte Carlo method. The form-factor itself is derived from a fit to the transverse distribution (Fig. 3) of the excess charge in the shower. The agreement between the Monte Carlo and analytic spectra are good at low frequencies (< 10 GHz). Fig. 3 shows the Monte Carlo frequency spectrum from a 100 GeV shower.

There are several subtleties at the high frequency end of the spectrum. The linear coherence with shower energy does not translate to higher frequencies but some degree of coherence is retained. The scale of coherence is influenced by the peak (~ 0.1 cm) of the transverse distribution of the excess charge in the shower which is much smaller than the Moliere radius (~ 10 cm). However, understanding the high frequency behavior may involve addressing questions of the role played by the high energy particles at the beginning of the shower and the statistics of the signal phase relationships from different tracks in the later stages of the shower, for example.

D. Summary of Shower Simulations

We have updated our calculations previously done with the GEANT 3.21 default settings by using the preferred settings of GEANT 3.21 and GEANT 4. The new results yield considerably higher track lengths,

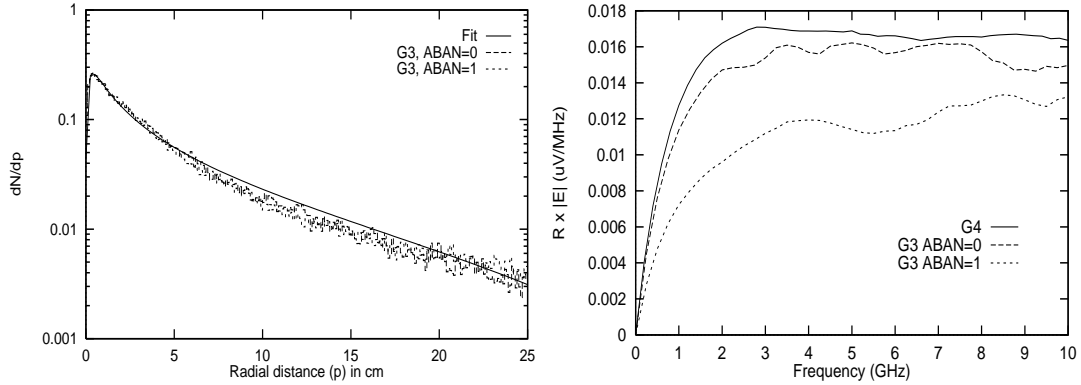


FIG. 4. Transverse excess charge distribution of a 100 GeV shower at the maximum [left panel] and the Monte Carlo frequency spectrum [right panel].

number of particles and electromagnetic signal strength. Antenna response is directly proportional to the electric field amplitude, which in turn affects the effective volume of the experiment.

We conclude that, for purposes of scaling radio signals from lower to higher energy showers, one can reasonably rely on linear scaling for frequencies below a few GHz. Clearly there is some interesting physics to explore in the domain above a few GHz. This important topic and the topic of signal contributions from the hadronic shower component are currently under study.

IV. LIMITS ON THE NEUTRINO FLUX INCIDENT ON THE EARTH

Although RICE has sensitivity to such physics as monopoles, topological defects, etc., the primary aim of the RICE experiment is detection of cosmological neutrinos. To select neutrinos, we require candidate events to: a) have at least 4 antenna channels registering 5σ excursions in their waveforms, b) pass quality-of-vertex cuts, c) have reconstructed vertex depths below 150 m, c) a hit geometry consistent(/inconsistent) with a conically-(/spherically-) emitting source. Five candidate events pass all software filters; for all five events, hand-scanning reveals at least one hit clearly inconsistent with the time domain antenna response expected for a true neutrino. After elimination of such spurious hits identified in the visual scan, all five candidate events reconstruct near the surface. Monte Carlo simulated waveforms (superimposed upon noise taken from data) are used to determine event selection efficiencies. Table II presents the results of our search.

A. Monte Carlo Effective Volume

The primary result of the Monte Carlo is an energy-dependent effective volume for detection of neutrinos. For a given input spectrum and integrated livetime, the expected number of detections is then readily determined. We compare this with the observed number of detections, and obtain an upper limit to the normalization of the input spectrum. The effective volume averaged over the August 2000 exposure, for example, is shown as the bold curve in Figure 5a). For $E_\nu = 100$ PeV, $V_{eff} \sim 1 \text{ km}^3$.

B. Results

Given the known experimental circuit gains and losses determined from an absolute calibration [6], the effective volume V_{eff} is calculated as a function of incident E_ν , as an exposure average of the detector configurations. The most important variable is the global discriminator threshold, which is adjusted to maintain an acceptable trigger rate under conditions of varying environmental noise. Knowing the total livetime for the full dataset (3500 hours), and based on observation of zero candidates, we calculate (Figure 5b) an upper limit on the incident ν flux, as a function of incident energy.

Shown is the older upper limit from RICE (Aug., 2000 data only), as well as the AMANDA [18], AGASA [19] and Fly's Eye [20] experiments (dashed). The predictions shown in the Figure are: (a)=Stecker &

Salamon [12] (b)=Protheroe [13], (c)=Mannheim (A) [14], (d)=Protheroe & Stanev [15], (e)=Engel *et al.* GZK-model [16]. Also shown is the Waxman-Bahcall upper-limit [17] (grey). For a given spectral shape, the integrated event rate depends only on the overall normalization, so limits shown replicate the shape of the test spectrum at an amplitude corresponding to the limit. Each RICE upper limit segment corresponds to the neutrino energy range responsible for the middle 80% of the event rate.

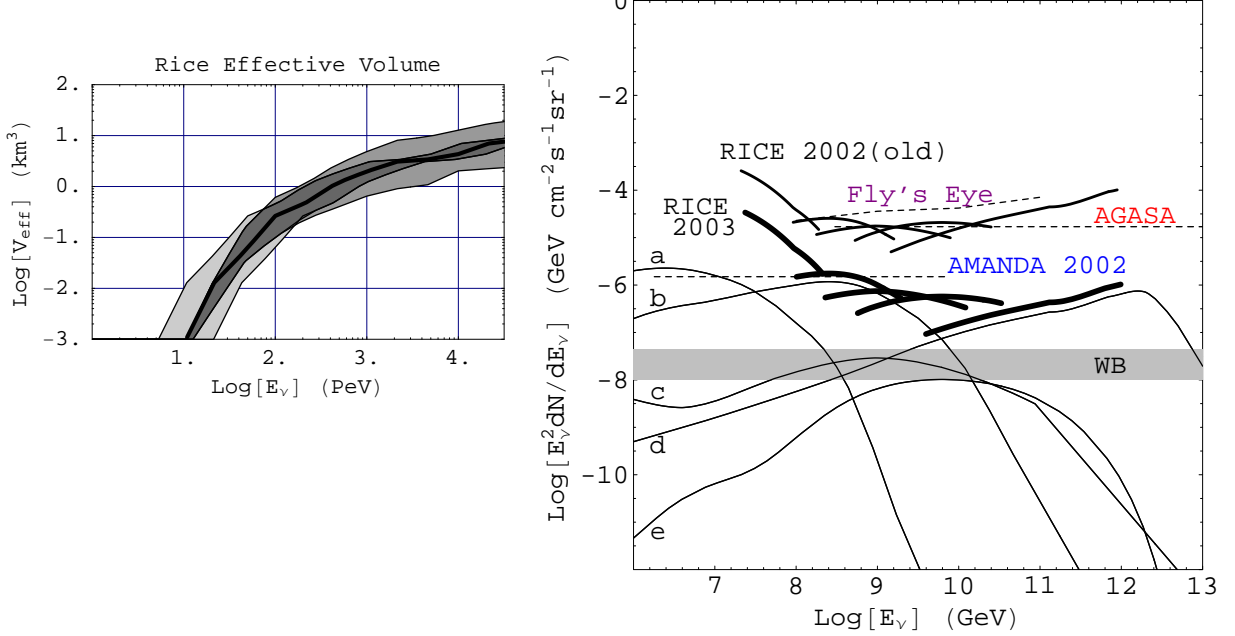


FIG. 5. LEFT: Effective volume, as a function of shower energy, for the August, 2000 data. The nominal result corresponds to the bold curve. The region in light gray spans the expected response due to variation in the attenuation length by factors of (0.5-2.0). The region in dark gray shows the range due to changes in signal strength by (0.5-2.0). RIGHT: Neutrino flux model predictions (a-e)) and corresponding current RICE calculated upper limits (95% confidence level; thick solid), as a function of E_ν .

Improvements in the RICE upper limit over the previous limit result from a nearly order-of-magnitude increase in the exposure, as well as inclusion of ν -induced hadronic showers.

Cut imposed	Surviving Data Events (1999/2000/2001)	MC events left
Total triggers	297512/111586842/3174390	400
Passing surface veto	12674/406867/97357	400
Passing $4 \times 5\sigma_V$ cuts	323/9001/9089	400
($Z < -150$ m)*(vertex quality) cut	5/177/68	396
Conical geometry	0/3/2	378
Passing Scanning	0/0/0	376

TABLE II. Summary of 1999-2001 data analysis.

C. Prospectus

In addition to searches for neutrinos, the RICE detector offers sensitivity to other analyses (monopole detection, studies of neutrinos coincident with GRB's and air showers, searches for micro-black holes, etc.); results of such searches will be reported in the future. The 2002 and 2003 datasets comprise our highest-quality data thus far and should offer substantial improvement over the results presented herein. Beginning in 2004, we hope to take advantage of the scientific opportunity presented by IceCube hole drilling to substantially expand the current RICE array.

V. IN SITU MEASUREMENT OF THE INDEX OF REFRACTION

A. Introduction

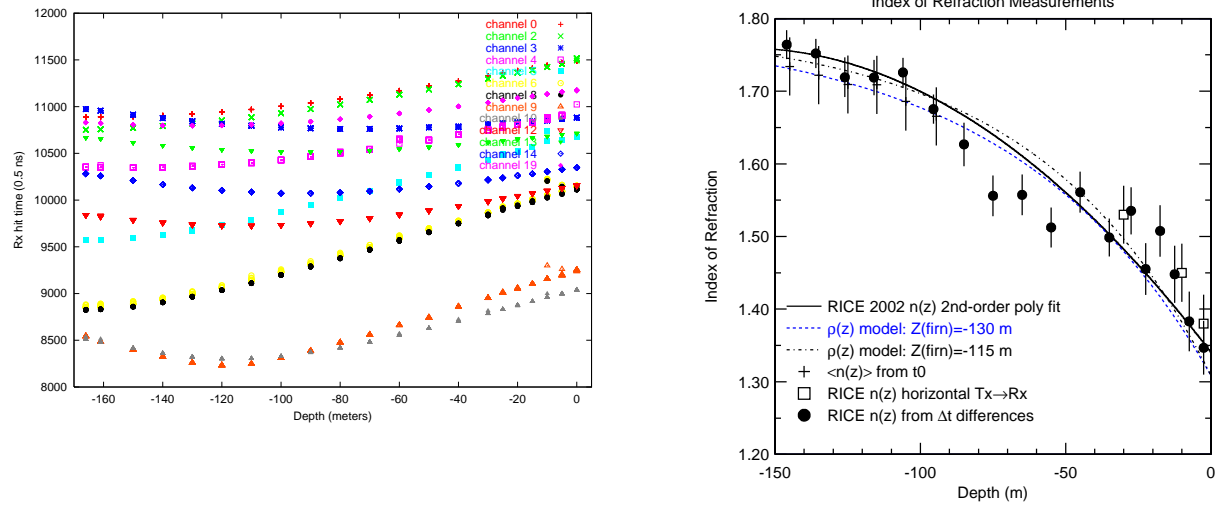
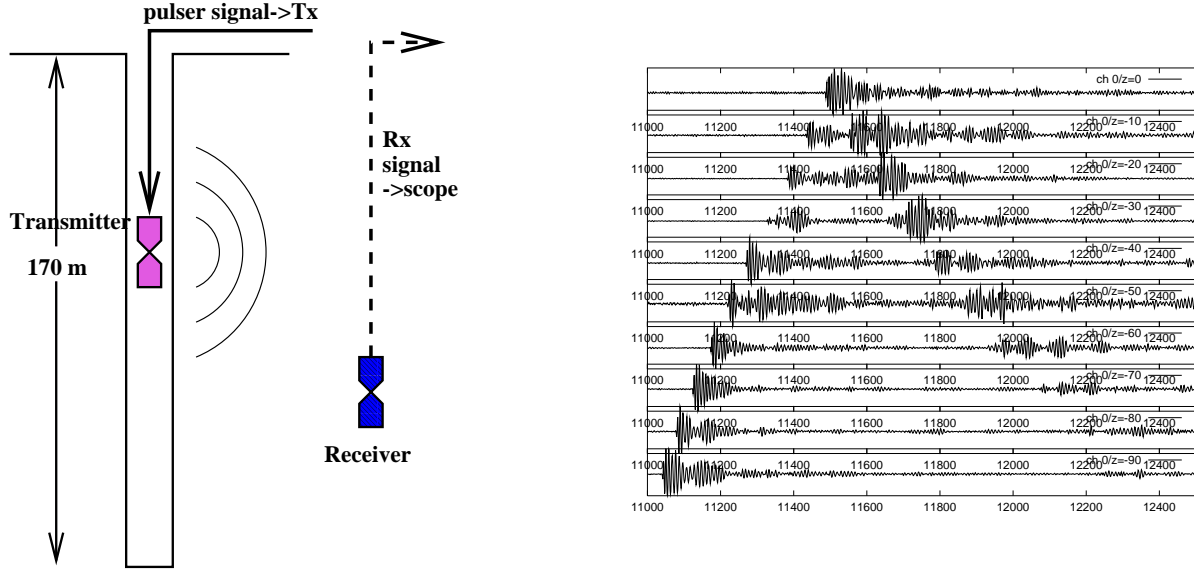
Whereas neutrinos are expected to interact below the array, RICE RF backgrounds due to air showers, or above-surface anthropogenic sources, require reconstruction of sources viewed upwards through the firn. Conversely, a receiver array deployed above the ice surface would also require ray tracing from in-ice neutrino interactions to the above-surface detector. This necessitates ray tracing the trajectories of radio waves through a region of variable ice density and dielectric constant, resulting in shorter signal propagation times and reduced signal amplitudes (at non-zero incident angles) compared to the case where sources are entirely below the firn.

B. Methods

Each RICE receiver consists of a half-wave dipole antenna, offering good reception over the range 0.2–1 GHz, plus a 36 dB low-noise amplifier. The peak response of the antenna is measured to be ~ 500 MHz in air (~ 300 MHz in ice), with a bandwidth $\frac{\Delta f}{f} \sim 0.2$. An identical dipole antenna, without the amplifier, is used as the transmitter for this measurement. As the transmitter was slowly lowered into a RICE borehole, a pulser signal was broadcast from the transmitter (at 5-10 meter depth increments) to the RICE receiver array, and signal arrival times in the receivers recorded (Figure 6). This afforded two measurements of the index of refraction: 1) the index of refraction as a function of depth ($n(z)$) could be inferred by determining the transit time difference to a particular receiver between successive transmitter locations ($n = c(t_{i+1} - t_i) / (|\vec{r}_{Tx, i+1} - \vec{r}_{Rx}| - |\vec{r}_{Tx, i} - \vec{r}_{Rx}|)$), and 2) the “mean” index of refraction ($\langle n(\Delta z) \rangle$), averaged over the distance from the transmitter to any receiver could be inferred by subtracting cable delays from the measured full circuit (pulse generator \rightarrow transmitter \rightarrow receiver \rightarrow DAQ) time. At each transmitter location, the t_0 of the transmitter signal, as well as an 8.192 microsecond waveform (sampled at 2 GSa/s) was recorded in an HP5452 digital oscilloscope, for each receiver. The hit time is determined from the first $\sim 5\sigma$ excursion in each waveform; the variation in receiver hit time with transmitter depth is shown in Figure 6b. As the transmitter approaches the (deeper) receiver, the hit time migrates to smaller values; also evident in the Figure are the “afterpulses” corresponding to signals which reflect off of the surface firn-air boundary, and back down to the buried receiver. As the transmitter is lowered to greater depths, the incident angle (with respect to normal surface incidence from the under-ice transmitter location) decreases and reflection effects correspondingly decrease, as well.

The local electromagnetic wave propagation velocity is directly obtained from successive hit times such as in Figure 6b, and can therefore be translated into an index-of-refraction profile, $n(z)$. Figure 7a) shows the locus of hit times for several receiver channels; the local value of $n(z)$ can be obtained from slopes to these data points. We have attempted to obtain an “aggregate” estimate of $n(z)$ by: a) adding the raising-transmitter plus lowering-transmitter datasets, b) adding all “good” data from all possible channels, where the contribution to the final average from each channel was weighted by geometry (favoring nearly-vertical channels), c) averaging over possible transmitter location uncertainties by rebinning data and re-obtaining averages using 20 m distance differences (rather than 10 m) between successive Tx broadcasts. In all cases, we assumed a transmitter location uncertainty of 0.5 m for all measurements, as well as a hit-time uncertainty of 1 ns. Fig. 7b) shows the result of this procedure, and also includes data obtained by broadcasting horizontally between a transmitter-receiver pair being lowered simultaneously into two neighboring boreholes. Also included are measurements derived from the “average” $n(z)$ values obtained using absolute t_0 measurements, as well as comparisons with the predictions of the Schytt model [22], which relates index of refraction directly to firn density $\rho(z)$, assuming that the ice-firn transition occurs at either $z = -115$ m or $z = -130$ m.

The RICE data points are fit to a 2nd-order polynomial, with the constraint that the value of index of refraction at large depths approach a constant asymptotic value. We obtained an estimate of that asymptotic value by broadcasting from the deepest buried RICE transmitter down to the deepest buried RICE receiver over a distance of 233.4 m; both of these antennas are presumably well below the firn-ice transition. The measured propagation time is 1369 ± 8 ns, corresponding to $n = 1.764 \pm 0.021$. This value is in fair agreement with the accepted value of 1.78, as obtained by several measurements. The overall error (statistical + systematic) of each data point is estimated at 4%.



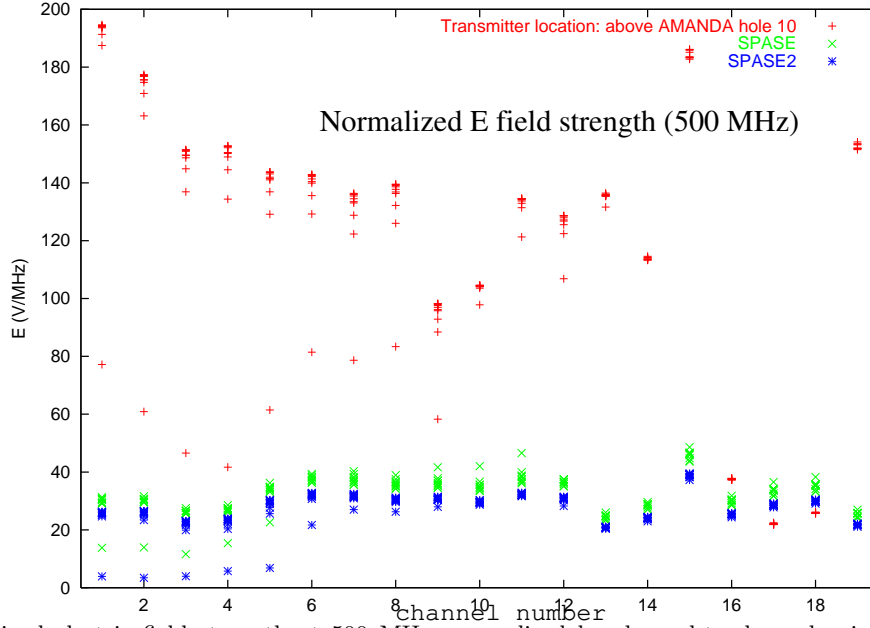


FIG. 8. Received electric field strength at 500 MHz, normalized by channel-to-channel gain, and corrected for distance-to-transmitter, for data taken with: a) (red) transmitter 3 meters above ice surface, and located above AMANDA hole 10; amplitude of output signal strength = 0.3 V, b) (green) transmitter 3 meters above ice surface, and located close to SPASE building at South Pole, approximately 350 meters (measured along the surface) from the center of the RICE receiver array; amplitude of output signal strength = 0.3 V, c) (blue) transmitter 3 meters above ice surface, and located close to SPASE building at South Pole, amplitude of output signal strength = 1 V; received power has been scaled by 1/3 to compare with a) and b). Note the agreement between the red vs. green/blue points for channels 16/17/18, which are receivers located in air and therefore immune to reflection effects.

C. Check of derived $n(z)$ using an amplitude analysis

The variable index-of-refraction of the firn has another important experimental consequence, due to the fact that any change in the index of refraction will introduce non-zero reflections at the corresponding interface. In any region where there is a variation in the index of refraction, reflection and transmission amplitudes, for both the perpendicular and parallel components of the incident electric field, are given by the standard “Fresnel coefficients” for dielectric media [23]: $r_{\perp} = -\sin(\theta_i - \theta_t)/\sin(\theta_i + \theta_t)$, $r_{\parallel} = +\tan(\theta_i - \theta_t)/\tan(\theta_i + \theta_t)$, $t_{\perp} = 2\sin(\theta_t)\cos(\theta_i)/\sin(\theta_i + \theta_t)$, $t_{\parallel} = 2\sin(\theta_t)\cos(\theta_i)/(\sin(\theta_i + \theta_t)\cos(\theta_i - \theta_t))$, as qualitatively illustrated in Figure 6b. Thus, the measured signal strength of above-ice sources, as viewed by below-firn receivers (or vice versa), depends on the degree of variation in the index of refraction. We have used this principle to check the derived index of refraction based on amplitudes alone.

To investigate firn transmission effects, we have broadcast to the RICE array from a surface point in the center of the RICE array (on top of AMANDA hole #10), compared to a point having a high inclination angle relative to the RICE array (in the vicinity of the SPASE building, approximately 350 meters in r away from the center of the RICE array). Figure 8 shows the results of this exercise, comparing measured electric field strengths, at the known broadcast CW frequency, and corrected for both receiver-to-receiver channel gain, as well as distance from transmitter to receiver. At each transmitter location, ten waveforms were captured, and the signal strength at 500 MHz obtained from a Fourier Transform of the time-domain signal. For the in-air horn antenna receivers, which are not subject to Fresnel losses, there is good agreement between the distant vs. the near source transmitter location data. However, broadcasting at large inclination angles from a more distant source point results in received signal strengths smaller by an order of magnitude than what can be accounted for by just $1/r$ and gain corrections. Our results are qualitatively consistent with the expected Fresnel coefficients [23]. However, a rigorous comparison with the Fresnel equations would require consideration of several effects, including: a) surface feature effects, b) evanescent waves which may propagate along the surface, and c) the true curvature of radio waves through the firn; we have not systematically evaluated such possible effects. Due to the latter uncertainty, no dipole field pattern geometry corrections have been applied – at relatively steep angles, such dipole field pattern corrections can be substantial. It should be noted that, in general, incorporating such corrections would have the effect of

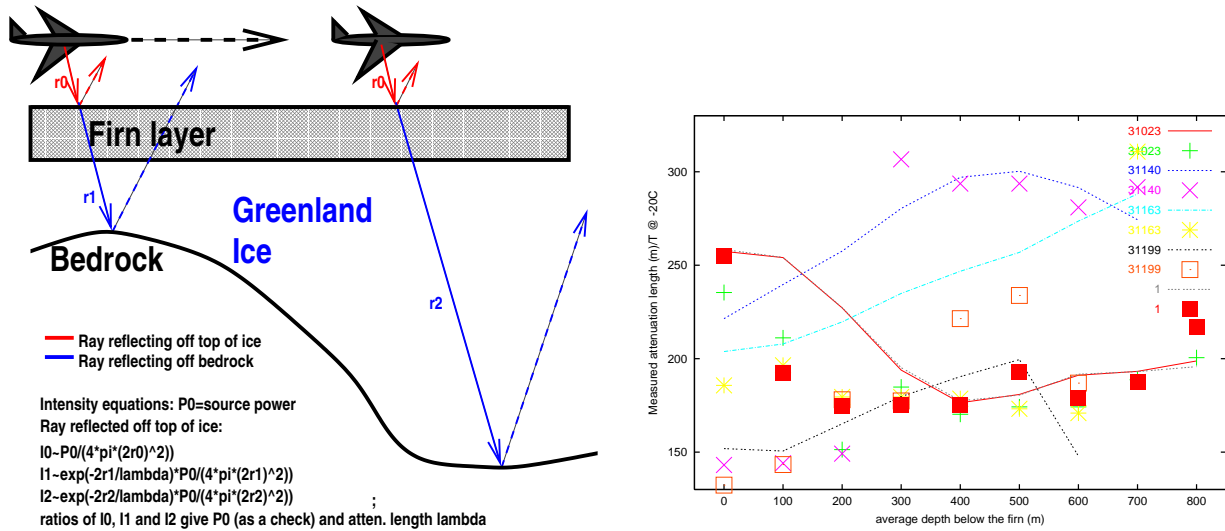


FIG. 9. a) LEFT: Schematic of ground-penetrating radar (GPR) measurements, used to estimate the radio-frequency ($f=150$ MHz) attenuation length, based on data taken by the KU group of Gogineni *et al.* We take the ratio of signal amplitudes returned by reflection off of bedrock beneath shallow ice vs. deep ice to infer the attenuation length at intermediate depths (plotted horizontally, and shown on the RIGHT (b)), for several different data runs. Although the scatter from run-to-run is large, results ($\lambda_{atten} \sim 250$ m) are in general agreement with previous estimates at this frequency and for this temperature.

increasing the disparity between the red vs. green/blue data points.

D. Estimate of attenuation length from Greenland data

We have estimated the attenuation length in warmer (-20 C) Greenland ice, using GPR data taken by the KU group of Gogineni *et al* in Greenland [24]. Here, we use the relative ratios of “return” signal strengths from a transmitter, on a low-flying plane, broadcasting signals off the under-ice bedrock (i.e., comparing the ratio of signal strength of the bedrock echo at different locations) to extract λ_{atten} . As indicated in Fig. 9, our initial estimates of the attenuation length from these data are encouraging and in agreement with previous measurements at these temperatures and wavelengths. With the larger array size afforded by IceCube, a direct *in situ* measurement using RICE receivers and transmitters should be straightforward.

VI. ACKNOWLEDGMENTS

We gratefully acknowledge the support of The Research Corporation, the NSF Office of Polar Programs under grant #OPP-0085119, as well as the University of Kansas Undergraduate Research Awards. The RICE experiment would not have been possible without the generous logistical and material support of the AMANDA Collaboration. We gratefully acknowledge additional support from the KU General Research Fund and the KU Research Development Fund, the New Zealand Marsden Foundation, and the Research Corporation.

-
- [1] <http://icecube.wisc.edu>
 - [2] <http://www.phys.hawaii.edu/~gorham/ANITA/ANITA.html>
 - [3] Evans, S. 1965, *J. Glaciol.* **5** (42), 773-792; Hempel L., Thyssen, F. *et al*, 2000, *J. Glaciol.*, 773
 - [4] Price B., 1996, *Astropart. Phys.* **5** **43**.

- [5] Kravchenko, I. *et al.*, astro-ph/0206371, accepted by Astropart. Phys.;
- [6] Kravchenko, I. *et al.*, 2003, Astropart.Phys. 19, 15-36.
- [7] Razzaque S. *et al.* 2002, Phys. Rev. D65, 103002
- [8] Zas E., Halzen F., Stanev T., 1991, *Phys. Rev.* **D45**, 432
- [9] Zas E., Halzen, F., Stanev, T. 1992, Phys. Rev. D45, 362
- [10] Alvarez-Muñiz J. *et al.* 2002, arXiv:astro-ph/0206043
- [11] Alvarez-Muñiz J. *et al.* 2002, arXiv:astro-ph/020604
- [12] Stecker F. & Salamon M., 1996, *Space Sci. Rev.* **75**
- [13] A. P. Szabo and R. J. Protheroe, Astropart. Phys. 2, 375 (1994); R. J. Protheroe and A. P. Szabo, Phys. Rev. Lett. 69, 2285 (1992).
- [14] Mannheim, K., 1995, *Astropart. Phys.* **3**, 295
- [15] Protheroe, R. J., 1997, ASP Conf. Series V. 121, 585
- [16] Engel R., Seckel D. and Stanev T. (2001), *Phys. Rev.* **D64:093010**.
- [17] Waxman, E. and Bahcall, J., 1999, *Phys. Rev.* **D59:023002**, and (2001) *Phys. Rev.* **D64:023002**
- [18] Ahrens, J. *et al.* (AMANDA), 2002, *Phys. Rev.* **D67:012003**.
- [19] Yoshida, S. *et al.* (AGASA), 2001, Proc. 27th ICRC, Vol. 3, 1146.
- [20] Balusaitas, R. *et al.* (Fly's Eye), 1995, *Phys. Rev.* **D31**, 2192.
- [21] Andres, E. *et al.*, 2000, *Astropart. Phys.* 13, 1
- [22] Schytt, V., 1958, *Glaciology* 2, 115.
- [23] M. Born and E. Wolf, Principles of Optics, Pergammon Press, 1964
- [24] <http://tornado.rsl.ukans.edu>